Swansea University
Prifysgol Abertawe

Cronfa
Setting Research Free

Cronfa - Swansea University Open Access Repository

This is an author produced version of a paper published in:
Nano Energy

Cronfa URL for this paper:
http://cronfa.swan.ac.uk/Record/cronfa44424

Paper:
Wang, R., Wang, C., Feng, Y. & Tang, C. (2018). Mechanisms underlying the shape effect on nano-piezoelectricity.
Nano Energy
http://dx.doi.org/10.1016/j.nanoen.2018.09.031

This item is brought to you by Swansea University. Any person downloading material is agreeing to abide by the terms of the repository licence. Copies of full text items may be used or reproduced in any format or medium, without prior permission for personal research or study, educational or non-commercial purposes only. The copyright for any work remains with the original author unless otherwise specified. The full-text must not be sold in any format or medium without the formal permission of the copyright holder.

Permission for multiple reproductions should be obtained from the original author.

Authors are personally responsible for adhering to copyright and publisher restrictions when uploading content to the repository.

http://www.swansea.ac.uk/library/researchsupport/ris-support/

Author's Accepted Manuscript

Mechanisms underlying the shape effect on nano-piezoelectricity

R.J. Wang, C.Y. Wang, Y.T. Feng, Chun Tang

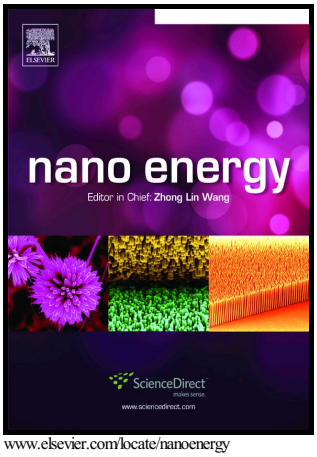

www.elsevier.com/locate/nanoenergy

PII: S2211-2855(18)30675-X
DOI: https://doi.org/10.1016/j.nanoen.2018.09.031
Reference: NANOEN3036

To appear in: *Nano Energy*

Received date: 19 July 2018
Revised date: 6 September 2018
Accepted date: 14 September 2018

Cite this article as: R.J. Wang, C.Y. Wang, Y.T. Feng and Chun Tang, Mechanisms underlying the shape effect on nano-piezoelectricity, *Nano Energy,* https://doi.org/10.1016/j.nanoen.2018.09.031

This is a PDF file of an unedited manuscript that has been accepted for publication. As a service to our customers we are providing this early version of the manuscript. The manuscript will undergo copyediting, typesetting, and review of the resulting galley proof before it is published in its final citable form. Please note that during the production process errors may be discovered which could affect the content, and all legal disclaimers that apply to the journal pertain.

ACCEPTED MANUSCRIPT

Mechanisms underlying the shape effect on nano-piezoelectricity

R.J. Wang[1], C.Y. Wang[1*], Y.T. Feng[1], Chun Tang[2]

[1]Zienkiewicz Centre for Computational Engineering, College of Engineering, Swansea University, Bay Campus, Swansea, SA1 8EN, UK

[2]Faulty of Civil Engineering and Mechanics, Jiangsu University, No. 301 Xuefu Road, Zhenjiang, Jiangsu, P.R. China 210013

*Corresponding author: chengyuan.wang@swansea.ac.uk

Accepted manuscript

Abstract

Piezoelectric nanowires (NWs) or nanotubes (NTs) are a vital component in nano-electromechanical and piezo-electronic device development. With various cross-sectional geometries achievable, the piezoelectric property-cross sectional shape relation is of fundamental interest. As existing studies (primarily based on first-principles calculations) are limited to ultrathin NWs or analysis based on continuum theories, the present work employs molecular statics (MS) simulation, which enables the examination of NWs/NTs up to cross-sectional size of 20.6*nm* and elucidation of the underlying mechanisms at the atomic level. Analyses are carried out for NWs/NTs with experimentally observed geometry by comparing their size-dependence of effective piezoelectric constant and the radial distribution of the average dipole moment change with strain. The fraction of strain-sensitive dipoles, initial volume contraction and surface piezoelectricity were shown to control the shape effect on the piezoelectricity of ZnO nanostructures.

Keywords: Zinc oxide Nanowires, shape effect, piezoelectric constants, volume contraction

ACCEPTED MANUSCRIPT

1. Introduction

The development of piezoelectric nanostructures (PNs), in the recent decade, has led to practical ambient energy harvesters critical for self-powered nano-electronics [1,2] and provided an avenue towards prospective innovations in sensing [3], actuation [4], piezotronics [5,6] and biomechanical energy extractors [7]. A great deal of the effort has been devoted towards predicting the mechanical [8–11] and especially, piezoelectric behaviors and properties [12–20] of one-dimensional PNs. e.g. wurtzite zinc oxide (ZnO) and gallium nitride (GaN) nanowires (NWs), which is of importance to fundamental research and practical application due to the combined semiconducting-piezoelectric nature [5] and the diverse range of the stable growth structures with distinct shape of the cross section [21]. Particular attention has been placed on the size and related surface effect on the material properties of NWs due to the potential for property tailoring.

Ensuing the seminal demonstration of NW piezo-response by Wang *et. al.* [22,23], experimental studies have shown size induced enhancement of effective piezoelectric coefficients (PZC) in ZnO nanostructures [24,25]. The inverse PZC size effect in NWs (i.e., higher PZC at smaller size) is then established with corroboration of first-principles studies of ultrathin (< 3*nm*) [0001]-oriented hexagonal ZnO NW (h-NW) [14,26–28]. Nevertheless, the discrepancy in the quantitative characterization of the size-effect remained, which, in the key work by Qin *et. al.* [29], is attributed to the different definitions of PZC and the effective volume. Indeed, through re-evaluation under one appropriate definition, a monotonous inverse size-effect (sizes < 3*nm*) with similar PZC values can be achieved across all studies [29].

However, the examination of PZC size effect for nanostructures beyond 5*nm* in size was only made viable by Dai *et. al.* in [30] where the validity of classical core-shell potential in bulk ZnO piezoelectric response modelling was first demonstrated. Subsequently, Molecular statics

ACCEPTED MANUSCRIPT

and dynamics studies were conducted by the same group to study ZnO (0001) surface piezoelectricity [31] and the influence of its effect on the overall PZC for finite-sized, square ZnO NWs (s-NWs) [16]. More relevantly, the s-NW PZC was found to exhibit a proportional dependence on size in opposition to the h-NW trend, which pinpoints to a crucial cross-sectional shape effect on piezoelectric property. Very recently, substantial shape effect on PZC is also achieved for GaN NW PZC by Lu *et. al.*, based on a continuum model [32]. This, to the best of our knowledge, is one of a few recent studies where the shape effect, a fundamental issue in the research of nano-piezoelectricity, has been examined in-depth. As the interplay between size effect and cross-sectional shape becomes increasingly important at the nanoscale, systematically exploring how these two factors couple and thereby influence the nano-piezoelectricity of ZnO NWs is essential to the understanding of the underlying physics. It is also expected to provide guidance for experimental efforts to fabricate high efficiency nano energy devices based on nanostructured ZnOs.

In addition to observing the shape effect, Lu et.al., [32] further identified specific surface area as the determining parameter in the shape effect on nano-piezoelectricity. Thus, it is of value for fundamental study to take advantage of atomistic simulation and investigate the mechanisms at atomic level underlining the shape effect and its relation to the specific surface area. To do so we adopt ZnO as a prototypical example and an MS method similar to [30,33] to study the axial PZC variations across differently shaped ZnO nanostructures and characterize the intrinsic shape effect. Particularly, to remove the influence from different facet structures, we consider in this study experimentally observed ZnO nanostructures with facets dominantly composed of the same crystallographic planes.

Accepted manuscript

ACCEPTED MANUSCRIPT

2. Molecular statics simulation

In order to examine the effect of shape on nanostructure piezoelectric property, the most prevalent ZnO nanostructures with the same growth orientation, $[0001]$ or c-axis, and dominant facets consisting the $\{01\bar{1}0\}$ planes were modelled [21,34]. The cross-sectional shapes of the structures considered are presented in Fig. 1a – d, which sequentially corresponds to an h-NW, a hexagonal nanotube (h-NT), a triangular NW (t-NW) and a nanobelt (NB). The comparability of the different structures is established through adopting a characteristic size such that the outer (lateral) surface areas are equal for all nanostructures at the same size (Note that h-NT inner surfaces are not accounted). Thus, considering the bulk lattice constants, we define the diameter d of h-NWs, side length b of t-NWs, outer diameter d_0 of h-NTs and width w (the thickness $t = w/2$) of NBs as the characteristic size k. At the same characteristic size, i.e., $k = d = b = d_o = w$, all these structures with equal length l possess the same area of outer surfaces, i.e., $3kl$. In addition, the inner diameter d_i of 2.6*nm*, 5.2*nm* and 10.5*nm*, is considered for h-NTs. The cross-sectional dimensions of all specimens are presented in Table. 1.

The atomic interaction is modelled via a core-shell Buckingham potential constructed by Binks and Grimes [35]. The validity of the potential in computational study of linear piezoelectric properties for bulk ZnO has been demonstrated by Dai *et. al.* [30]. It was further applied to model free surface piezoelectric response for ZnO (0001) surface, NBs and h-NWs [16,31,36]. The detailed formulation is as follows:

$$E = \sum_i \sum_{j>i} A \cdot exp(-r_{ij}/\rho) - C{r_{ij}}^{-6} + E_{long}(r_{ij}) \quad (1)$$

where r_{ij} is the distance between an atom pair and A, C, ρ are parameters for the pair-wise interaction. The parameter values are taken from [35] and the r_{ij} cut-off is set at 1.2*nm*. Due to

ACCEPTED MANUSCRIPT

the existence of free surfaces the electrostatic interactions are computed utilizing the approach of Fennel and Gezelter [37], which improved upon Wolf's summation by ensuring potential and force continuity at the cut-off radius:

$$E_{long} = \sum_i \sum_{\substack{j>i \\ r_{ij}<r_c}} q_i\, q_j \left[\frac{erfc(\alpha r)}{r} - \frac{erfc(\alpha r_c)}{r_c} + \left(\frac{erfc(\alpha r_c)}{{r_c}^2} + \frac{2\alpha}{\sqrt{\pi}}\frac{exp(\alpha^2 {r_c}^2)}{r_c}\right)(r - r_c)\right] \qquad (2)$$

where q_i and q_j are the partial charges; α is the damping coefficient and r_c the cut-off radius respectively, and their values of 0.33 and 1.5*nm* are selected based on the convergence of piezoelectric property studied.

The LAMMPS software suite [38] is utilized to conduct the simulated uniaxial deformation and the molecular statics method is employed to exclude thermal fluctuation. Periodic boundary condition is enforced in the axial direction to remove end effects. At zero strain, the initial local minimum energy structure is found through energy minimization via the conjugate gradient method. Engineering strain is then applied at increments of 0.5% up to ±1% and relaxed at each strain via the same method. The relaxed structure is utilized in the calculation of the axial polarization. The deformation experienced by the structure can be separated into the applied homogeneous strain and internal strain. The latter results from the structural relaxation required to reach an energy minimized state after each applied strain.

The c-axis or axial polarization, P_3, can be decomposed in general into the electron delocalization and the internal strain terms of Eqn. 3.

$$P_3 = P_3(u(\varepsilon_3), \varepsilon_3) = P_3^{elec}(\varepsilon_3) + P_3^{dis}\big(u(\varepsilon_3)\big) \qquad (3)$$

Here, the internal strain term $P_3^{dis}\big(u(\varepsilon_3)\big)$ is the polarization contribution from the relative displacement between the zinc and oxygen atoms, which is reflected through the change in fractional atomic coordinate u. The $P_3^{elec}(\varepsilon_3)$ or electron delocalization effect is represented

Accepted manuscript

ACCEPTED MANUSCRIPT

through the core shell separation [30]. To compute the P_3 of each nanostructure (i.e., supercell), the volume normalized polarization, $\bar{P}_3 = P_3/V$, is adopted where V is the volume of the corresponding nanostructure (similar to [33]). As the cross sections are simple shapes the volume can be effectively calculated by the volume of an equivalent continuous structure that encompasses the energy minimized structure. The cross-sectional area is defined by the area bounded by the contour formed through adjoining the centers of the outmost atoms as illustrated by the black outlines in Fig. 1b, c and d for h-NT, t-NW and NB. For all structures the length is determined by the length of the simulation box in the c-axis direction. Finally, the piezoelectric response of the nanostructures are characterized by an effective piezoelectric constant for the axial (c-axis) direction. We employ the method of [30,33] based on the proper piezoelectric constant definition introduced by Vanderbilt [39].

$$e_{33}^{eff} = \frac{\partial \bar{P}_3}{\partial \varepsilon_3} \quad (4)$$

Accepted manuscript

3 Results and discussion

In this section, the MS simulations demonstrated above are performed to characterise the shape effects on the axial PZC, e_{33}^{eff}, of ZnO nanostructures and disclose the physical mechanisms underlying the effect of the cross-sectional shapes on the size-dependence of the PZC. Four ZnO nanostructures are considered including h-NWs, h-NTs and t-NWs as well as NBs.

3.1 Shape effect on the size dependence of e_{33}^{eff}

To study the shape effect, we first calculate the characteristic size-dependence of e_{33}^{eff} in Fig. 2 for all nanostructure types considered. Expectedly, in Fig. 2, the dependence of e_{33}^{eff} on the

characteristic sizes for all nanostructures examined hold an inverse relationship and show at least a 28% enhancement (at 20.6*nm*) compared to the bulk value of 1.624 C/m^2. The obtained trend of h-NW e_{33}^{eff} is found to be consistent with previous first-principles and MD studies [14, 28, 29, 33] for ultrathin NWs. However, the NB trend opposes the findings in [33]. This mainly stems from the difference in the structures of $\{1\bar{1}00\}$ facet examined in the two studies, which results in the difference in surface reconstruction, the determining factor in the size dependence of NB e_{33}^{eff} [33].

The impact of cross-sectional shape on e_{33}^{eff} is clearly observed in Fig. 2 through the relative difference in e_{33}^{eff} and its rate of change with the size between the structures. Using h-NWs (Fig. 1) as benchmark, t-NWs exhibit larger e_{33}^{eff} values at all sizes with 10% rise at 4.9*nm* and 3% at 20.6*nm*. For h-NTs, an even higher gain of 21.5% compared to h-NWs (17.5% versus t-NW) is obtained at the size of 4.9*nm*. However, as its e_{33}^{eff} decays most rapidly with the increasing size, e_{33}^{eff} of h-NT quickly declines below the t-NW response at the size of around 7*nm* or larger, and finally approaches the h-NW value at 12.8*nm*. To summarize, for the sizes below 7*nm*, h-NTs exhibit the highest e_{33}^{eff}, h-NWs the lowest value and that of t-NWs is in between. Above 7*nm*, t-NWs show the largest e_{33}^{eff} while those of h-NWs and h-NTs are lesser and tend to get closer to each other with raising size. The NB e_{33}^{eff} trend line closely tracks the h-NW benchmark relation with relative difference around 0.5%. The size-dependence of the specific surface areas are shown in the inset of Fig. 2 for all structures considered. The trends are found to be similar to those of e_{33}^{eff} in Fig. 2.

It is noted that the cross-sectional shape of h-NT contains additional dimension, i.e., the inner diameter d_i or the thickness t $(= (d_o - d_i)/2)$. Thus, further calculations are performed

Accepted manuscript

to identify the determining parameter for e_{33}^{eff}. In Fig. 3, the d_o-dependence of h-NT e_{33}^{eff} is represented by three solid lines associated with constant d_i of 2.6*nm*, 5.2*nm* and 10.5*nm*, respectively, while the three dashed lines denote the d_i-dependence of h-NT e_{33}^{eff} corresponding to the thickness, $t = 1.2nm$, 2.1*nm* and 5.1*nm*, respectively. It is seen from the three dashed lines that e_{33}^{eff} decreases greatly with the rising thickness. The small d_i-dependence is also observed for the thin h-NTs with t = 1.2*nm* but becomes negligible at t > 2.1*nm*. In addition, since there are only two independent factors among d_0, d_i and t the large d_0-dependence associated with constant d_i (i.e., the three solid lines in Fig.3) also reflects the sensitivity of h-NT e_{33}^{eff} to the change of the thickness t. It is thus concluded that the thickness t is the key factor that controls e_{33}^{eff} of h-NTs. The influence of d_i (or d_o) is observable only for ultra-thin h-NTs with thickness 1.2*nm*, i.e., four atom layers. Again, in the inset of Fig. 3, the trends of the specific surface area change with the size is plotted, which are quite close to their counterparts of e_{33}^{eff}.

Here, the shape effect shown in Fig. 2 is obtained for periodic axial boundary condition or infinitely long ZnO nanostructures where the end effects (or aspect ratio effect) on the deformation and material properties are excluded. However, ZnO nanostructures of finite length are used in their applications with certain constraints imposed on their two ends. It is thus of practical interest to further examine the possible effect of end constraints or the aspect ratio on the e_{33}^{eff}. To this end, we calculate the aspect ratio-dependence of e_{33}^{eff} for h-NWs (d = 4.7*nm*) and t-NWs (b = 7*nm*) with finite length and nearly equal specific surface area (~0.09). In particular, four atom layers at each ends of structures are fixed to restrict their displacements in all directions and thus model the clamped ends for ZnO nanostructures. Here, the average volume per Zn-O dimer V_a needs to be calculated in evaluating e_{33}^{eff} of the nanostructures. For

Accepted manuscript

ZnO nanostructures with periodic boundary condition V_a can be easily obtained as the nanostructures are perfect hexagonal cylinders and experience a uniform deformation when subjected to tensile force. However, when a finite length and fixed ends are concerned it is not that straight forward to calculate the volume as the end effect leads to non-uniform structural relaxation (before a force is applied) and deformation (when subjected to a tensile force). An appendix is thus attached to show the calculation methods for the finite-length nanostructures with clamped ends. The results obtained are presented in Table 5 showing that e_{33}^{eff} of the h-NWs increases from 2.157 C/m^2 at the aspect ratio 2.1 to 2.335 C/m^2 at the aspect ratio 10, and approaches the value 2.361 C/m^2 of infinitely long *h*-NWs when the aspect ratio further increases. A similar trend is observed for the t-NWs and consistent with Fig.2, e_{33}^{eff} of the t-NWs is higher than the one of the h-NW at nearly equal specific surface area. We note that a minor overestimation of e_{33}^{eff} by around 1% at larger aspect ratio are observed due to the approximation method used in evaluating V_a of t-NWs. The relative change of e_{33}^{eff} achieved for the h-NWs and t-NWs is 8.6% and 4.5%, respectively, when the aspect ratio grows from around 2 to infinitely large. It is understood that aspect ratio-dependent e_{33}^{eff} arises from the constraints imposed on the two ends. Its influence on nano-piezoelectricity however is observable but small. As such, the trend shown in Fig.2 should remain nearly the same for the nanostructures of a finite length and with differently constrained ends.

In the above analyses, the shape effect on the size dependence of e_{33}^{eff} are achieved for the four different nanostructures considered. Specifically, the role of the specific surface area in the size and shape effect of e_{33}^{eff}, and the key factor t for the piezoelectrical effect of h-NTs are identified for the ZnO nanostructures. The possible end effect on e_{33}^{eff} is also examined for ZnO

Accepted manuscript

nanostructures. Here, comparison to experimental data is challenging as existing experiments [40-44] are mainly focused on the piezoelectric constant d_{33}^{eff} for the inverse piezoelectric effect of ZnO NWs, NBs or nanorods [40-44] instead of e_{33}^{eff} obtained here. In addition, synthesized ZnO nanostrucutres typically yield sizes from hundreds of nanometers [42, 44] to micrometers [40]. The smallest ZnO h-NWs achieved in experiments have a diameter around 50*nm* [42], which is still much larger than the maximum 20*nm* size considered here. For these large nano-, meso- or micro-piezoelectrical structures, the shape or size effect on nano-piezoelectricity almost vanishes. This can be understood from Fig.2 where the shape or size effect decreases substantially with rising size or specific surface area. Specifically, large uncertainty arises in the experiments with the obtained values of d_{33}^{eff} ranging from 1 to 45*pm*/*V* [40-44] due to the crystallographic defects in the fabricated NWs and different magnitudes [40] or frequencies [41] of the external loads applied in individual experiments. These however are not considered in the present MS simulations. As a result, a direct comparison cannot be achieved between the shape or size-dependence of e_{33}^{eff} obtained in the present simulations and the available experimental data. In the meantime, first-principles calculations [12, 14, 18, 26-28] (for ultra-thin nanostructures), molecular dynamics simulations (MDSs) [19, 20, 30, 31] and a continuum model [32] have been efficiently used as an alternative way to investigate the size effect or shape effect on piezoelectricity of small pristine nanostructures that cannot be easily synthesized experimentally. We, therefore, form comparison with the previous simulations and theoretical models in predicting the size and shape effects on nano-piezoelectricity. It is shown that the shape effect on ZnO nanostructures and the importance of thickness *t* for ZnO h-NTs obtained in this work agrees qualitatively with MDSs [19, 20] and the most recent theoretical model [32] for GaN nanostructues. The trend of e_{33}^{eff} to size change is also found to be consistent with the first-

Accepted manuscript

ACCEPTED MANUSCRIPT

principles calculation for ultrathin ZnO and GaN NWs [14,28,29], e.g., the diameter from 0.6*nm* to 2.4*nm* [14]. It is thus of great interest to further explore the physical origins behind the observation at atomic level, and reveal their pathway to generate the shape-dependent piezoelectricity at the nanoscale. These are of scientific and engineering interest and considered as fundamental issues in the research of nanomaterial and nanomechanics.

3.2. Physical mechanisms of the shape effect

As shown by Qin *et.al.* [18], the e_{33}^{eff} description is given by Eqn. 6, which is adopted here to characterize the cross-sectional shape effect.

$$e_{33}^{eff} = \partial(P_{3a}/V_a)/\partial\varepsilon_3 = (\partial P_{3a}/\partial\varepsilon_3) * V_a^{-1} + (\partial V_a^{-1}/\partial\varepsilon_3) * P_{3a} \qquad (6)$$

Here, ε_3 is the axial strain, P_{3a} is the average dipole moment per Zn-O dimer. The evaluation of all quantities in Eqn. 6 is presented in Tables 2, 3 and 4 for t-NWs, h-NTs and h-NWs, respectively. As shown in Tables 2 to 4, amongst the structures considered $(\partial P_{3a}/\partial\varepsilon_3) * V_a^{-1}$ is between 2.45 C/m^2 and 3.23 C/m^2 which is around one order of magnitude greater than the absolute value of $(\partial V_a^{-1}/\partial\varepsilon_3) * P_{3a}$ varying from 0.27 to 0.41 C/m^2. More importantly, $(\partial P_{3a}/\partial\varepsilon_3) * V_a^{-1}$ is found to be much more sensitive to the shape variation than is $(\partial V_a^{-1}/\partial\varepsilon_3) * P_{3a}$. Therefore, to extract the origins of the shape effect on e_{33}^{eff} we shall focus our attention on its dominant part $(\partial P_{3a}/\partial\varepsilon_3) * V_a^{-1}$.

3.2.1 Shape effect due to surface layer

In this section, we first discuss the physical orgins of the shape effect (Sec.3.1) from the surface layers. It is noted in Tables 2 and 3 that, for h-NTs compared with t-NWs, the difference of $(\partial P_{3a}/\partial\varepsilon_3) * V_a^{-1}$ (or e_{33}^{eff}) at small characteristic size mainly arises from the

Accepted manuscript

variation of V_a^{-1} (inverse average volume) while $\partial P_{3a}/\partial \varepsilon_3$ remains nearly unchanged. For example, for h-NT versus t-NW of 4.9*nm*, $\partial P_{3a}/\partial \varepsilon_3$ is slightly lower (~3%) but V_a^{-1} is much greater (~10%) leading to higher $(\partial P_{3a}/\partial \varepsilon_3) * V_a^{-1}$ (or e_{33}^{eff}) of the h-NT. It is understood that V_a^{-1} reflects the initial volume contraction arising primarily from residual surface stress whose effect can be enhanced by raising the specific surface area**.** As shown in the inset of Fig. 2, at the small size (< 6*nm*) t-NTs with inner and outer surfaces exhibit much higher specific surface area, which naturally leads to much greater residual surface stress. The higher surface stress finally results in larger initial volume contraction and thus, greater e_{33}^{eff} of h-NTs. It is thus concluded that, as far as larger specific surface area is considered, the initial volume contraction due to the residual surface stress plays an central role in determining the shape effect on nano-piezoelectricity.

In addition, it is noted in Tables 2 to 4 that, across the three nanostructures studied, both $\partial P_{3a}/\partial \varepsilon_3$ and V_a^{-1} decrease with the rising characteristic size or the decreasing specific surface area (See the insets in Figs. 2 and 3). Specifically, V_a^{-1} of h-NTs (Table 3) is found to decrease more rapidly than V_a^{-1} of t-NWs (Table 2) while the rate of change in $\partial P_{3a}/\partial \varepsilon_3$ are quite close. As a result, when the size increases, $(\partial P_{3a}/\partial \varepsilon_3) * V_a^{-1}$ (or e_{33}^{eff}) of h-NTs decreases more rapidly than that of t-NWs. It finally becomes lower than that of t-NWs (Table 2) and approaches its counterpart of h-NWs (Table 4) at sufficiently large size. These results closely reflect the shape effect on e_{33}^{eff} achieved in Fig. 2 for t-NWs, h-NTs and h-NWs. It is thus confirmed that the transition from around 10% e_{33}^{eff} enhancement to about 3% reduction of h-NTs (relative to e_{33}^{eff} of t-NWs) shown in Fig.2 is attributable to the quicker decay of volume contraction of h-NTs with the decreasing specific surface area.

Accepted manuscript

Indeed, the initial volume contraction (V_a^{-1}) and its sensitiveness to the variation of the specific surface area are found to play a central role in determining the shape effect on e_{33}^{eff} of h-NTs and t-NWs. As mentioned above, this volume contraction is mainly due to the residual surface tension and thus considerably decreases with the decreasing specifc surface area. It is however independent of the effect of surface piezoelectricity in ZnO nanostructures. These results and analyses eventually converge to the fact that the residual surface stress is one of the major determinants of piezoelectricial effect at the nanoscale and it impacts the nano-piezoelectricity by enhancing the volume contraction of nanostructure to improve dipole moment per unit volume.

For the shape-effect between h-NW and NB an oddity occurs as at the same size the values of e_{33}^{eff} are near parity (Fig.2) while the specific surface area are up to ~30% larger for NBs (Fig. 2 inset). The additional $\{11\bar{2}0\}$ surface planes in NBs seem to suggest an obvious explanation in difference of surface layer behaviour, however, a comparison of the terms in Eqn. 6 shows additional effects. The evaluated Eqn. 6 terms are presented in Table 6 for h-NW and NB sizes of 7.5 and 12.1 nm. First, term A is larger by 1-~1.6% in NBs owing to larger V_a^{-1} and coheres with their greater specific surface areas. However, term B (negative) is also smaller for NBs by 10-15% due to a larger absolute values of $\partial V_a^{-1}/\partial \varepsilon_3$. Therefore, the more sensitive volume change to strain competes with the effect from higher specific surface area in NBs resulting in the marginal e_{33}^{eff} shape-effect observed between h-NWs and NBs.

3.2.2 Shape effect from internal layers

Next, let us find out the physical origin of the shape effect from the internal layers by comparing t-NWs with h-NWs. It is found in Tables 2 and 4 that $(\partial P_{3a}/\partial \varepsilon_3) * V_a^{-1}$ (or e_{33}^{eff}) of t-NWs is greater across the characteristic sizes considered. V_a^{-1} of t-NWs is, however, very close

Accepted manuscript

to that of h-NWs. For example, at the size of 4.9nm $\partial P_{3a}/\partial \varepsilon_3$ and V_a^{-1} of t-NWs are, respectively, 8% and 2% higher, which decreases to 2.6% and 0.5% at 20.6nm (Tables 2 and 4). Thus, the larger $(\partial P_{3a}/\partial \varepsilon_3) * V_a^{-1}$ of t-NWs is primarily due to its greater $\partial P_{3a}/\partial \varepsilon_3$.

To reveal the polarization mechanism underlining the above t-NW versus h-NW shape effect, we further calculate $(\partial P_{3a}/\partial \varepsilon_3)^l$ for each concentric Zn-O layer that maintains the cross-sectional geometry of the corresponding nanostructures. The surface and sub layers are defined as the outermost and the subsequent interior Zn-O layers. All remaining interior layers are referred to as core layers. The results are presented in Figs. 4 and 5 for h-NWs and t-NWs. Here, the innermost core layer is denoted as layer 1. The outer layers are labelled by integers in ascending order when moving outwards in the radial direction.

For an h-NW, $(\partial P_{3a}/\partial \varepsilon_3)^l$ of the core layers is nearly a constant which rises gradually with growing size but is always below the bulk value 3.55 eÅ (Fig. 4). It then abruptly increases above the bulk at the sub (by ~3-6%) and surface layers (by ~21%). Differently, in t-NWs $(\partial P_{3a}/\partial \varepsilon_3)^l$ of layer 1 reaches its maximum value around 27% higher than the bulk. It then decays rapidly in the neighbouring 3 to 4 layers (Fig. 5). After that, it decreases gradually to finally reach its minimum value above 3.55 eÅ. At the sub and surface layers, the sudden increase of $(\partial P_{3a}/\partial \varepsilon_3)^l$ occurs, which is up to around 21% higher than the bulk. This rapid growth in $(\partial P_{3a}/\partial \varepsilon_3)^l$ at the surface layers is found to be very similar in both t- and h-NWs. The surface piezoelectricity thus can contribute to the shape-dependence on e_{33}^{eff} when the fraction of surface Zn-O dipoles (measured by the specific surface area) is different between the two NWs. In contrast, $(\partial P_{3a}/\partial \varepsilon_3)^l$ distributions across the core layers are substantially different in the two NWs. Thus, the different distributions should contribute largely to the disparity in the overall $\partial P_{3a}/\partial \varepsilon_3$ between the two NWs. The change made by the distinct distributions can be

Accepted manuscript

substantial even if the two NWs have the same specific surface area. For example, for h-NW of 4.9*nm* and t-NW of 6.7*nm* while the specific surface areas are nearly equal (Fig. 2 inset) the t-NW e_{33}^{eff} is noticeably higher than the h-NW value (Fig. 2).

Here, it is worth mentioning that $(\partial P_{3a}/\partial \varepsilon_3)^l$ distribution is substantially different for h-NWs (Fig.4) and t-NWs (Fig.5) no matter what characteristic size is considered. This leads to different overall value of $(\partial P_{3a}/\partial \varepsilon_3)^l$ for the two NWs at the small size. Nevertheless, with the rising size the overall values of the two NWs will get closer to each other and finally converge to the bulk value at sufficiently large size. This is simply because the contribution of the surface layers and the central layers of the t-NWs to the overall $(\partial P_{3a}/\partial \varepsilon_3)^l$ value decreases and then vanishes when the size is raised to a sufficiently large value.

To understand the different $(\partial P_{3a}/\partial \varepsilon_3)^l$ distribution, we examine the structural details of h- and t-NWs. Their core layers form hexagonal and triangular shells, respectively, with the length equal to *l*. The cross-sectional views of the shells (viewed in the axial direction [0001]) are shown in Fig. 6a and b. For a core layer of h-NWs (Fig. 6a), a four-atom unit (highlighted in green in Fig. 6c) can be viewed on the lateral surfaces of the shell in $[0\bar{1}10]$ direction. This unit is the repeating unit of h-NW layers, which shows four Zn-O dipoles denoted by their displacement vectors (in the direction of tensile strain) as $\boldsymbol{n}_0$, $\boldsymbol{n}_1$, $\boldsymbol{n}_2$ and $\boldsymbol{n}_3$, respectively (Fig. 6c). For a core layer of t-NWs (Fig. 6b), the same repeating units are found between the corners of its triangular cross-section, while, at the corners a six-atom repeating unit is achieved (Fig. 6d) in the axial direction [0001]. The shape effect on these two NWs thusly lies in the different corner structures of t-NWs where the six-atom units possess additional Zn-O dipoles denoted by $\boldsymbol{n}_1'$, $\boldsymbol{n}_2'$ and $\boldsymbol{n}_3'$ (Fig. 6d).

Accepted manuscript

As verification of this explanation, we re-calculate the $(\partial P_{3a}/\partial \varepsilon_3)^l$ distribution for the 4.9*nm* t-NW by excluding the contribution from the additional corner Zn-O dipoles (Fig. 6d) within all t-NW core layers. The distribution is plotted in Fig. 7 in comparison with the 4.9*nm* h-NW distribution. Evidently, the modified $(\partial P_{3a}/\partial \varepsilon_3)^l$ distribution of t-NW no longer exhibits a large increment against bulk value at its layer 1 (the innermost layer) and are nearly parity with h-NW values of 3.39 eÅ (below bulk). The results confirm that, for t- and h-NWs, different $(\partial P_{3a}/\partial \varepsilon_3)^l$ distributions are due to the extra Zn-O dipoles at the corner of t-NW layers (Fig. 6d).

In our simulations of tensile test, we calculate in Fig. 8 the axial displacements of all atoms in the relaxation after a (uniform) strain increment (See details in Sec.2). The results show that while n_0 reduces, c remains unchanged, leading to increased n_1', n_2' and n_3'. As such, n_1', n_2' and especially n_3' increases more sensitively to the tensile strain than does n_0, i.e., $\frac{\partial n_i'}{\partial \varepsilon_3} > \frac{\partial n_0}{\partial \varepsilon_3}$ (i = 1, 2 and 3). Here, n_i' represents the magnitude of $\boldsymbol{n}_i'$ (i = 1, 2 and 3) and the corresponding dipole moment is given by $q \cdot \boldsymbol{n}_i'$ where q is the charge of dimers independent of ε_3 (same for $\boldsymbol{n}_i$ in Fig. 6). Thus, the additional strain-sensitive dipole $\boldsymbol{n}_i'$ (i =1, 2 and 3) in the six-atom unit of t-NWs can greatly increase $(\partial P_{3a}/\partial \varepsilon_3)^l$ through higher $\frac{\partial n_i'}{\partial \varepsilon_3}$ (i=1, 2 and 3). The high sensitiveness of $\boldsymbol{n}_i'$ to an external strain ε_3 at least partially explains the mechanisms behind the enhancement of $(\partial P_{3a}/\partial \varepsilon_3)^l$ due to the additional Zn-O dipoles found in the six-atom units in t-NWs (Fig. 6d).

Conclusions

In this study, MS simulations and theoretical analyses are combined to examine the shape effect on the axial piezoelectric constant e_{33}^{eff} of ZnO nanostructures with an emphasis on its physical mechanisms. The atomic fraction of the strain-sensitive Zn-O dipoles, the initial volume

Accepted manuscript

contraction V_a^{-1} induced by residual surface stress and the surface piezoelectricity are identified as main physical origins leading to the (cross-sectional) shape-dependence of PZC. The impacts of these small-scale effects decrease with the rising characteristic size or the specific surface area of the ZnO nanostructures. On the other hand, the sensitivity of volume change to axial strain is high for NB and exerts significant influence on their piezoelectric effect independent of the specific surface area. The above results demonstrate that a sizable contribution to shape and size dependence of nano-piezoelectricity is not determined by the surface layers and thus, cannot be fully controlled entirely by the specific surface area.

At small characteristic sizes, h-NTs and t-NWs exhibit large specific surface area and thus higher residual surface stress. In this case, the surface layer-induced volume contraction V_a^{-1} plays a major role in determining the PZCs. As a result, h-NTs with larger volume contraction (i.e., higher V_a^{-1}) show greater e_{33}^{eff} than that of t-NWs. With rising size, V_a^{-1} of h-NTs however declines more rapidly than V_a^{-1} of t-NWs, giving lower e_{33}^{eff} in h-NT at relatively large size.

For t-NWs and h-NWs, the greater portion of the strain-sensitive Zn-O dipoles (i.e., those with larger displacement change due to an applied strain) in t-NWs greatly enhance their $\partial P_{3a}/\partial \varepsilon_3$ at the core layers, leading to greater e_{33}^{eff} of t-NWs. The portion of the strain-sensitive dipoles in t-NWs then decreases with the rising size but is always larger than its counterpart of h-NWs even if they have the same specific surface areas.

In addition, surface piezoelectricity responsible for the size effect on e_{33}^{eff} also contributes to the shape effect on e_{33}^{eff}. Its influence is implemented via the variation of the specific surface area induced by changing the cross-sectional shapes.

Accepted manuscript

ACCEPTED MANUSCRIPT

Appendix

Finite Length Nanostructure Volume Estimation

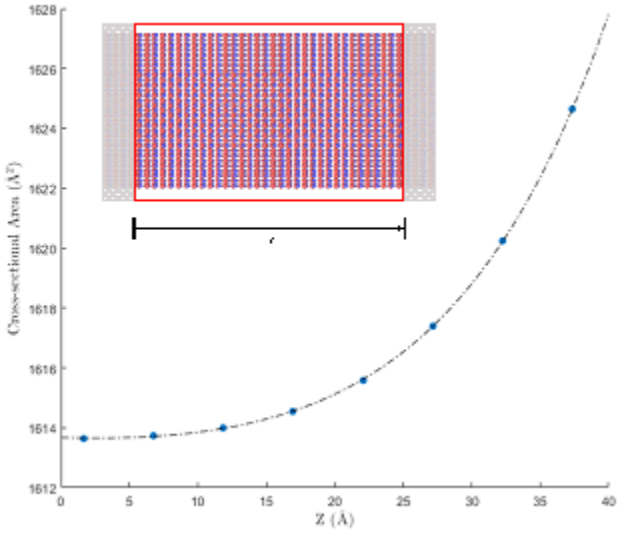

Figure 1. The cross-sectional area change along Z (blue dot) and exponentially fitted function (dot-dashed) line for h-NW of d=4.9nm and aspect ratio 1 at zero strain.

The volume of an encapsulating continuum body is again utilized to estimate finite nanostructure volume (Fig.1 marked in the red box) at each strain state. The layers of fixed atoms (grey) used to model clamped ends are not included. As the cross-sectional area varies along the nanostructure length in a symmetrical fashion, the cross-sectional areas are first estimated for at least 8 evenly spaced points along the nanostructure axial direction, z, for half of the nanostructure length. The cross-sectional area is calculated by a technique similar to section 2 via finding its bounding contours. The relationship between the cross-sectional area and z is then fitted by exponential functions for the examined length. For higher aspect ratios of 7.8 and 10, additional cross-sectional area evaluations are included in order to appropriately fit the exponential relation as the change in cross-sectional area become very rapid. The effective volume of the nanostructure is finally evaluated by integrating this fitted function across half of the nanostructure length and doubling its value.

Accepted manuscript

ACCEPTED MANUSCRIPT

References

[1] Wang Z L 2008 Towards self-powered nanosystems: From nanogenerators to nanopiezotronics *Adv. Funct. Mater.* **18** 3553–67

[2] Yang X and Daoud W A 2016 Triboelectric and Piezoelectric Effects in a Combined Tribo-Piezoelectric Nanogenerator Based on an Interfacial ZnO Nanostructure *Adv. Funct. Mater.* **26** 8194–201

[3] Chen Z, Wang Z, Li X, Lin Y, Luo N, Long M, Zhao N and Xu J Bin 2017 Flexible Piezoelectric-Induced Pressure Sensors for Static Measurements Based on Nanowires/Graphene Heterostructures *ACS Nano* **11** 4507–13

[4] Muralt P, Polcawich R G and Trolier-McKinstry S 2009 Piezoelectric thin films for sensors, actuators, and energy harvesting *MRS Bull.* **34** 658–64

[5] Wu W and Wang Z L 2016 Piezotronics and piezo-phototronics for adaptive electronics and optoelectronics *Nat. Rev. Mater.* **1** 16031

[6] Wang Z L 2010 Piezopotential gated nanowire devices: Piezotronics and piezo-phototronics *Nano Today* **5** 540–52

[7] Yang R, Qin Y, Li C, Zhu G and Lin Wang Z 2009 Converting Biomechanical Energy into Electricity by a Muscle-Movement-Driven Nanogenerator *Nanoletters* **9** 1201–5

[8] Agrawal R, Peng B and Espinosa H D 2009 Experimental-computational investigation of ZnO nanowires strength and fracture. *Nano Lett.* **9** 4177–83

[9] Wang R J, Wang C Y and Feng Y T 2017 International Journal of Mechanical Sciences Effective geometric size and bond-loss effect in nanoelasticity of GaN nanowires *Int. J. Mech. Sci.* **130** 267–73

[10] Wang J, Shen Y, Song F, Ke F and Liao X 2017 On the wurtzite to tetragonal phase transformation in ZnO nanowires *Nanotechnology* **28** 165705

[11] Wang R J, Wang C Y, Feng Y T and Tang C 2018 Mechanical responses of a-axis GaN nanowires under axial loads *Nanotechnology* **29**

[12] Li C, Guo W, Kong Y and Gao H 2007 Size-dependent piezoelectricity in zinc oxide nanofilms from first-principles calculations *Appl. Phys. Lett.* **90** 033108

[13] Majidi C, Chen Z, Srolovitz D J and Haataja M 2010 Spontaneous bending of piezoelectric nanoribbons: Mechanics, polarization, and space charge coupling *J. Mech. Phys. Solids* **58** 73–85

[14] Agrawal R and Espinosa H D 2011 Giant piezoelectric size effects in zinc oxide and gallium nitride nanowires. A first principles investigation *Nano Lett.* **11** 786–90

[15] Zhang J, Wang R and Wang C 2012 Piezoelectric ZnO-CNT nanotubes under axial strain and electrical voltage *Phys. E Low-dimensional Syst. Nanostructures* **46** 105–12

[16] Dai S and Park H S 2013 Surface effects on the piezoelectricity of ZnO nanowires *J.*

Accepted manuscript

ACCEPTED MANUSCRIPT

Mech. Phys. Solids **61** 385–97

[17] Zhang J, Wang C and Bowen C 2014 Piezoelectric effects and electromechanical theories at the nanoscale *Nanoscale* **6** 13314–27

[18] Qin C, Gu Y, Sun X, Wang X and Zhang Y 2015 Structural dependence of piezoelectric size effects and macroscopic polarization in ZnO nanowires: A first-principles study *Nano Res.* **8** 2073–81

[19] Zhang J and Meguid S A 2015 On the piezoelectric potential of gallium nitride nanotubes *Nano Energy* **12** 322–30

[20] Zhang J and Zhou J 2018 Humidity-dependent piezopotential properties of zinc oxide nanowires: Insights from atomic-scale modelling *Nano Energy* **50** 298–307

[21] Ding Y, Zhang F and Wang Z L 2013 Deriving the three-dimensional structure of ZnO nanowires/nanobelts by scanning transmission electron microscope tomography *Nano Res.* **6** 253–62

[22] Wang Z L and Song J 2006 Piezoelectric nanogenerators based on zinc oxide nanowire arrays. *Science* **312** 242–6

[23] Qin Y, Wang X and Wang Z L 2008 Microfibre-nanowire hybrid structure for energy scavenging *Nature* **451** 809–13

[24] Zhao M H, Wang Z L and Mao S X 2004 Piezoelectric characterization individual zinc oxide nanobelt probed by piezoresponse force microscope *Nano Lett.* **4** 587–90

[25] Zhu R, Wang D, Xiang S, Zhou Z and Ye X 2008 Piezoelectric characterization of a single zinc oxide nanowire using a nanoelectromechanical oscillator *Nanotechnology* **19** 285712

[26] Xiang H J, Yang J, Hou J G and Zhu Q 2006 Piezoelectricity in ZnO nanowires: A first-principles study *Appl. Phys. Lett.* **89** 87–90

[27] Mitrushchenkov A, Linguerri R and Chambaud G 2009 Piezoelectric properties of AlN, ZnO, and HgxZn1-xO nanowires by first-principles calculations *J. Phys. Chem. C* **113** 6883–6

[28] Hoang M T, Yvonnet J, Mitrushchenkov A and Chambaud G 2013 First-principles based multiscale model of piezoelectric nanowires with surface effects *J. Appl. Phys.* **113** 014309

[29] Qin C, Gu Y, Sun X, Wang X and Zhang Y 2015 Structural dependence of piezoelectric size effects and macroscopic polarization in ZnO nanowires: A first-principles study *Nano Res.* **8** 2073–81

[30] Dai S, Dunn M L and Park H S 2010 Piezoelectric constants for ZnO calculated using classical polarizable core–shell potentials *Nanotechnology* **21** 445707

[31] Dai S, Gharbi M, Sharma P and Park H S 2011 Surface piezoelectricity: Size effects in nanostructures and the emergence of piezoelectricity in non-piezoelectric materials *J. Appl. Phys.* **110** 104305

Accepted manuscript

ACCEPTED MANUSCRIPT

[32] Jiang H, Su Y, Zhu J, Lu H and Meng X 2018 Piezoelectric and pyroelectric properties of intrinsic GaN nanowires and nanotubes: Size and shape effects *Nano Energy* **45** 359–67

[33] Momeni K and Attariani H 2014 Electromechanical properties of 1D ZnO nanostructures: nanopiezotronics building blocks, surface and size-scale effects *Phys. Chem. Chem. Phys.* **16** 4522–7

[34] Yang K, She G W, Wang H, Ou X M, Zhang X H, Lee C S and Lee S T 2009 ZnO nanotube arrays as biosensors for glucose *J. Phys. Chem. C* **113** 20169–72

[35] Jason Binks D and Grimes R W 1994 The non-stoichiometry of zinc and chromium excess zinc chromite *Solid State Commun.* **89** 921–4

[36] Momeni K, Odegard G M and Yassar R S 2012 Finite size effect on the piezoelectric properties of ZnO nanobelts : A molecular dynamics approach *Acta Mater.* **60** 5117–24

[37] Fennell C J and Gezelter J D 2006 Is the Ewald summation still necessary? Pairwise alternatives to the accepted standard for long-range electrostatics *J. Chem. Phys.* **124** 1–12

[38] Plimpton S 1995 Fast Parallel Algorithms for Short – Range Molecular Dynamics *J. Comput. Phys.* **117** 1–19

[39] Vanderbilt D 2000 Berry-phase theory of proper piezoelectric response *J. Phys. Chem. Solids* **61** 147–51

[40] Lee H, Park J, Han S A, Lee D, Kim K B, Lee N S, Park J Y, Seo Y, Lee S W and Choi Y J 2012 The stress-dependent piezoelectric coefficient of ZnO wire measured by piezoresponse force microscopy *Scripta Mater.* **66** 101–4

[41] Momeni K, Asthana A, Prasad A, Yoke K. Yap Y K , Shahbazian-Yassar R 2012 Structural inhomogeneity and piezoelectric enhancement in ZnO nanobelts *Appl. Phys. A* **109** 95–100

[42] Broitman E, Soomro M Y, Lu J, Willander M and Hultman L 2013 Nanoscale piezoelectric response of ZnO nanowires measured using a nanoindentation technique *Phys. Chem. Chem. Phys.* **15** 11113.

[43] Khan A, Hussain M, Nur Q, Willander M and Broitman E 2015 Analysis of direct and converse piezoelectric responses from zinc oxide nanowires grown on a conductive fabric *Phys. Status Solidi A* **212** 579–84

[44] Dimitrios T, Serban L, Vlad-Andrei A, et al 2015 Piezoelectric properties of template-free electrochemically grownZnO nanorod arrays *Appl. Sur. Sci*. **356** 1214-20

Accepted manuscript

ACCEPTED MANUSCRIPT

Dr. Chengyuan Wang is a senior lecturer at the Zienkiewicz Centre for Computational Engineering, Swansea University, UK. He obtained his Ph.D. degree in Mechanical Engineering from the University of Alberta, Canada (2006) and then worked as a postdoctoral fellow at the Centre for Advanced Material Technology, Sydney University, Australia for nearly one year. His research is mainly focused on theoretical analysis and computer simulations of mechanical and electromechanical behaviour of nanomaterials, nanocomposites and the protein polymers in eukaryotic cells. The analyses are carried out based on molecular dynamics simulations, structural mechanics techniques and the continuum mechanics theories.

Ruijie Wang received his BASc with honours in Engineering Science from University of Toronto, Canada in 2014. He is currently a Ph.D student in the Zienkiewicz Centre for Computational Engineering, Swansea University under the supervision of Dr. Chengyuan Wang. His research interests mainly focuses on the study of nanomaterial, nano-mechanics and piezoelectricity.

Dr. Feng is a professor in computational engineering in the Zienkiewicz Centre at Swansea. Over the last 30 years, he has been actively involved in developing advanced computational techniques, including the finite element methods, and discrete or particle methods.

Accepted manuscript

Professor Chun Tang received his B.S. and Ph.D degrees from Nanjing University of Aeronautics and Astronautics in China. Before joining Jiangsu University in 2017, he worked as a Post-Doctoral Scholar and Associate Specialist at the University of Nevada Las Vegas and University of California Merced. His main research interest includes electromechanical coupling properties of novel materials and their applications in new energy devices.

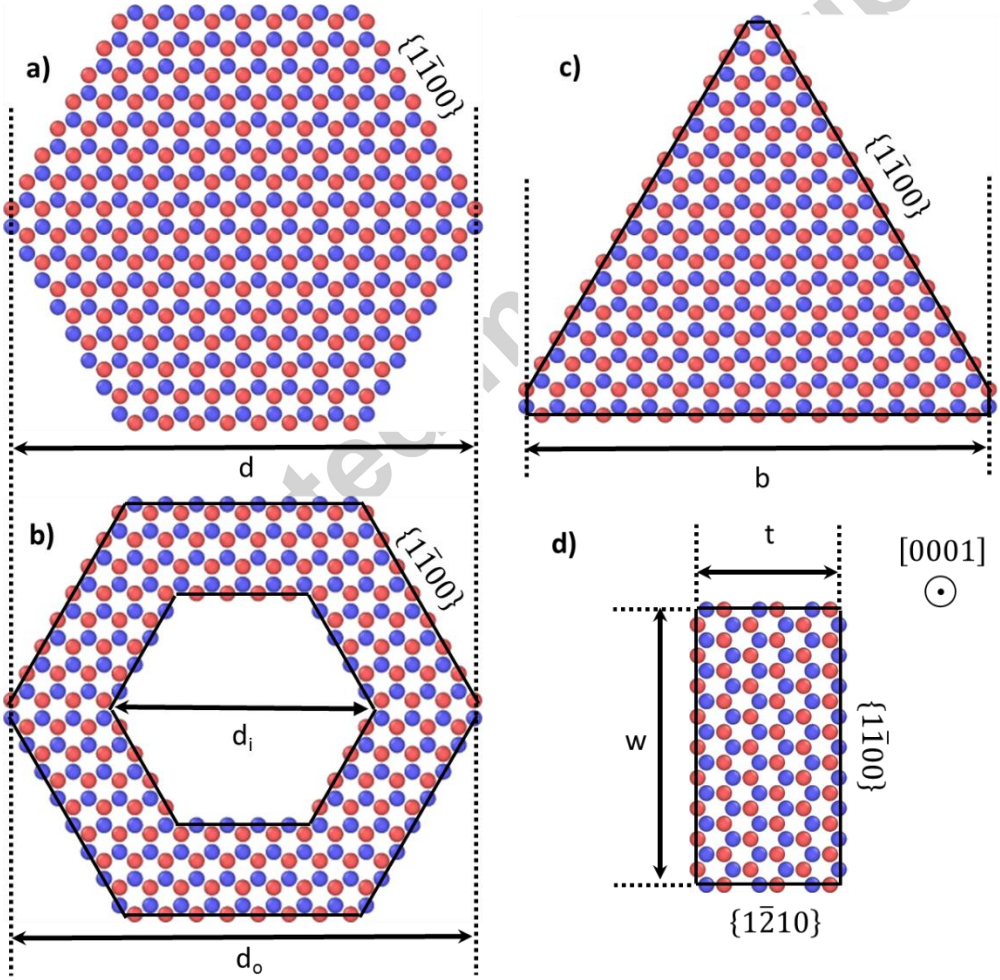

Figure 1. Cross-sectional geometry of all [0001] oriented nanostructures considered, where the black contour lines are the cross-sectional area boundary. a) h-NW, d is the diameter. b) h-NT, d_i

and d_o are the inner and outer diameters respectively (here $t = (d_o - d_i)/2$). c) t-NW, b is the base length. d) NB, t is the thickness and w the width.

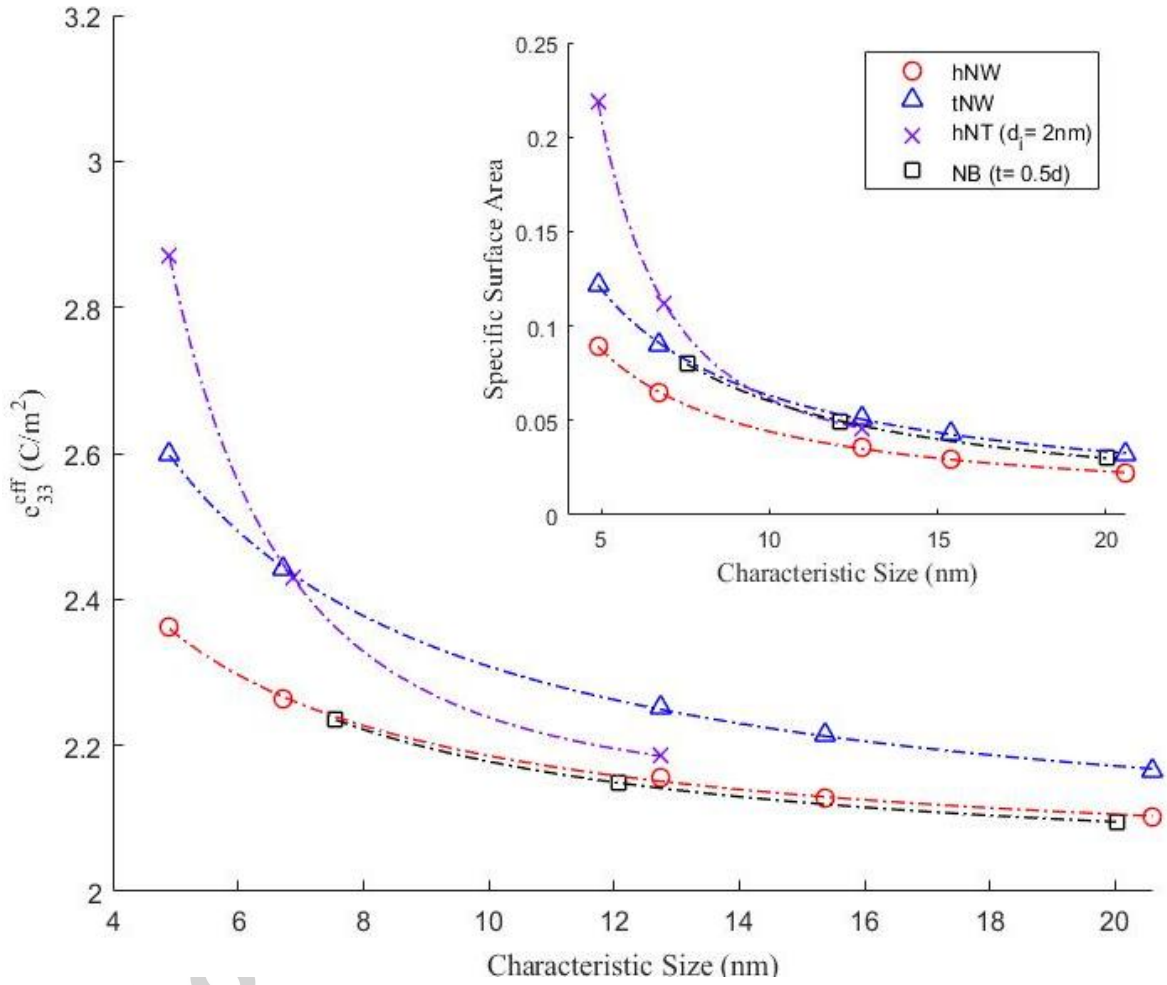

Figure 2. The change of e_{33}^{eff} with characterize size of all nanostructure types. The inset shows the specific surface area relation with characterize size.

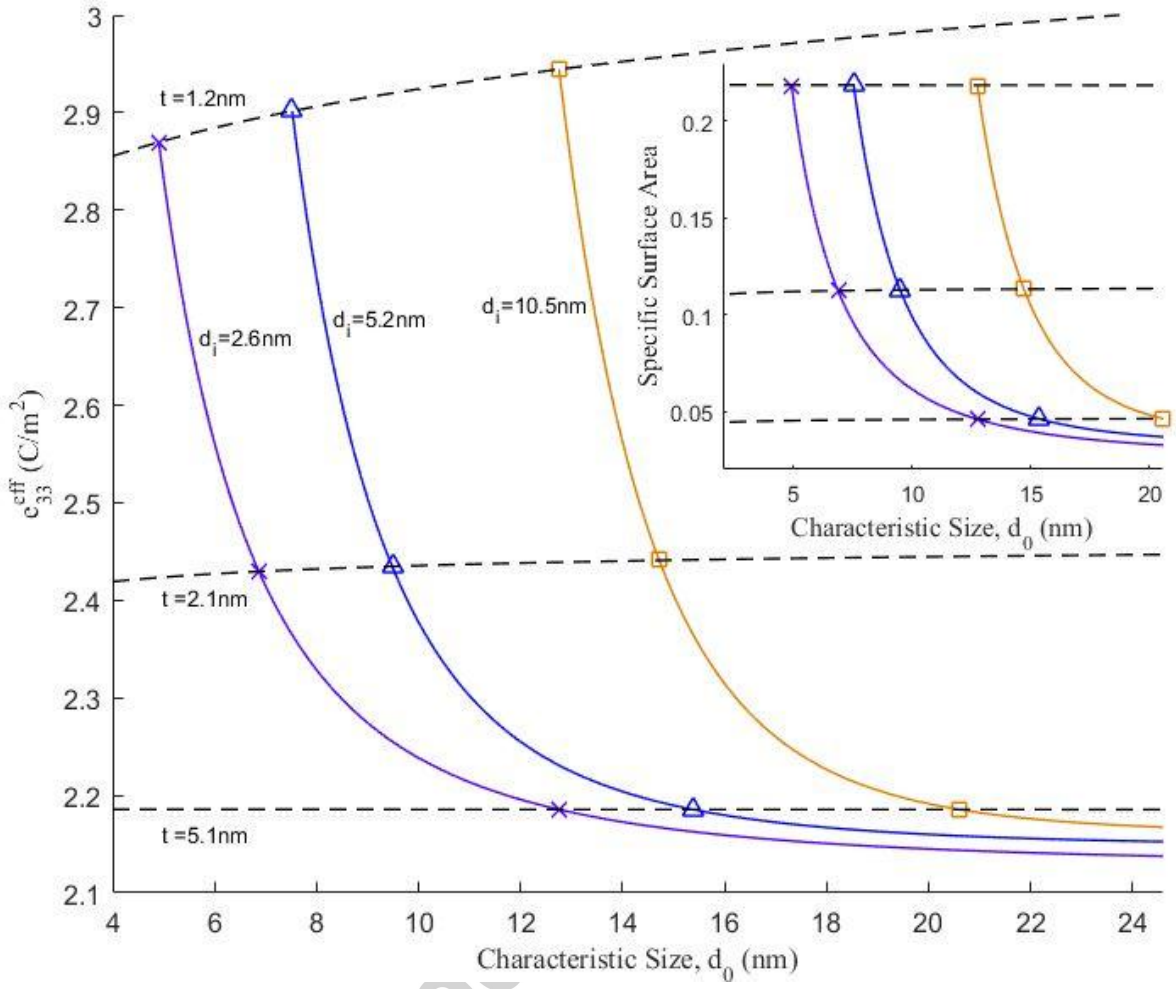

Figure 3. The change of e_{33}^{eff} with characterize size for all h-NTs considered.

Accepted

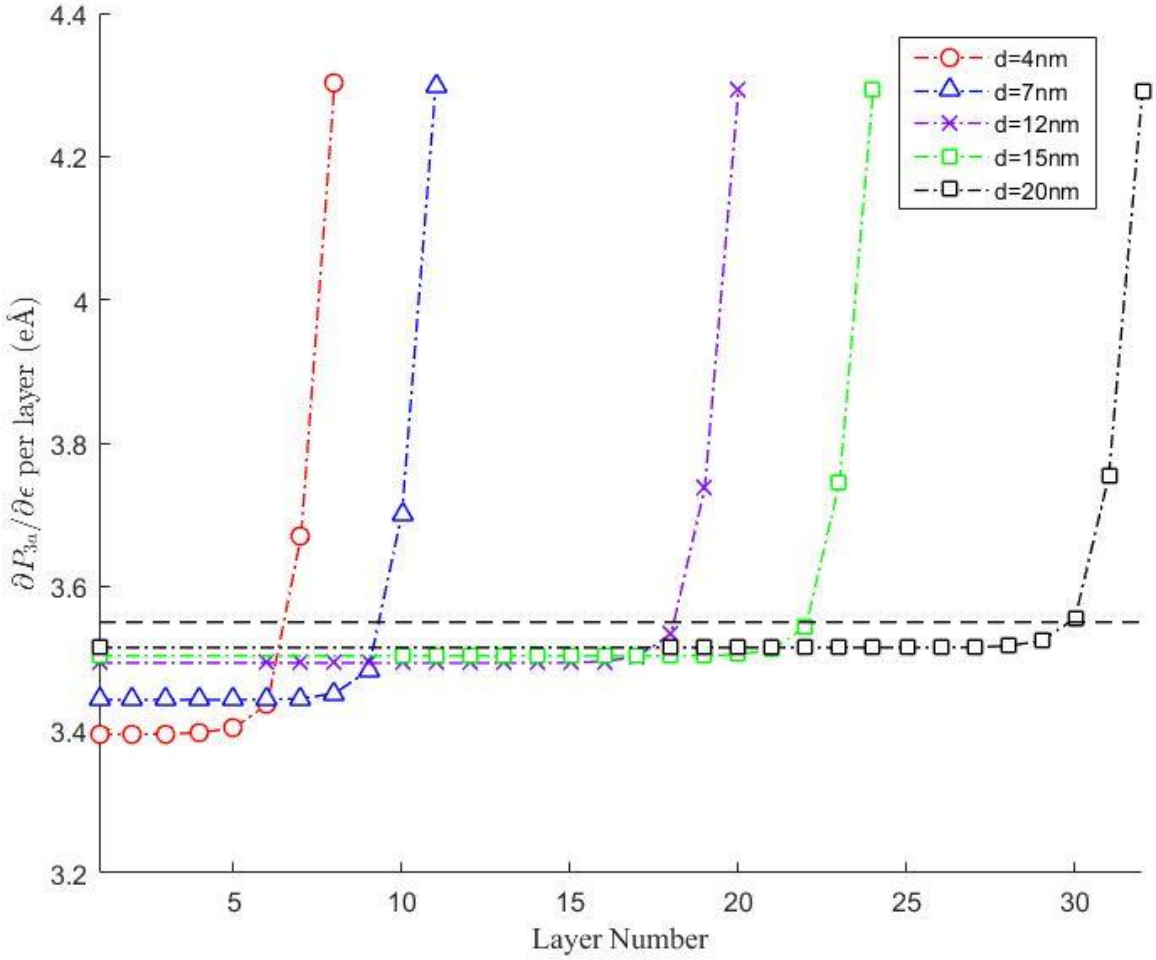

Figure 4. Radial distribution of $(\partial P_{3a}/\partial \varepsilon_3)^l$ for all h-NWs. The horizontal dashed line marks the bulk value of 3.55 eÅ.

Accepted

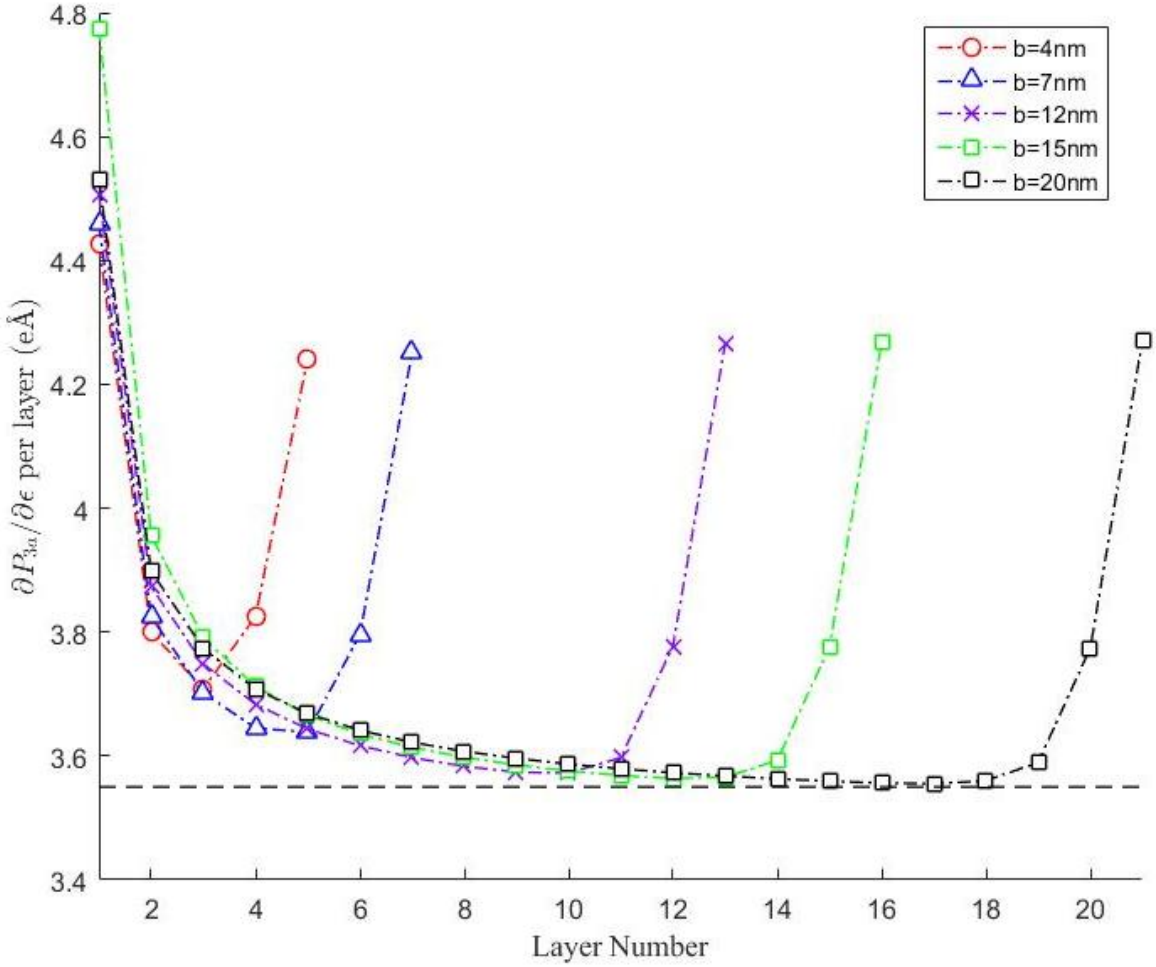

Figure 5. Radial distribution of $(\partial P_{3a}/\partial \varepsilon_3)^l$ for all t-NWs. The horizontal dashed line marks the bulk value of 3.55 eÅ.

Accepted

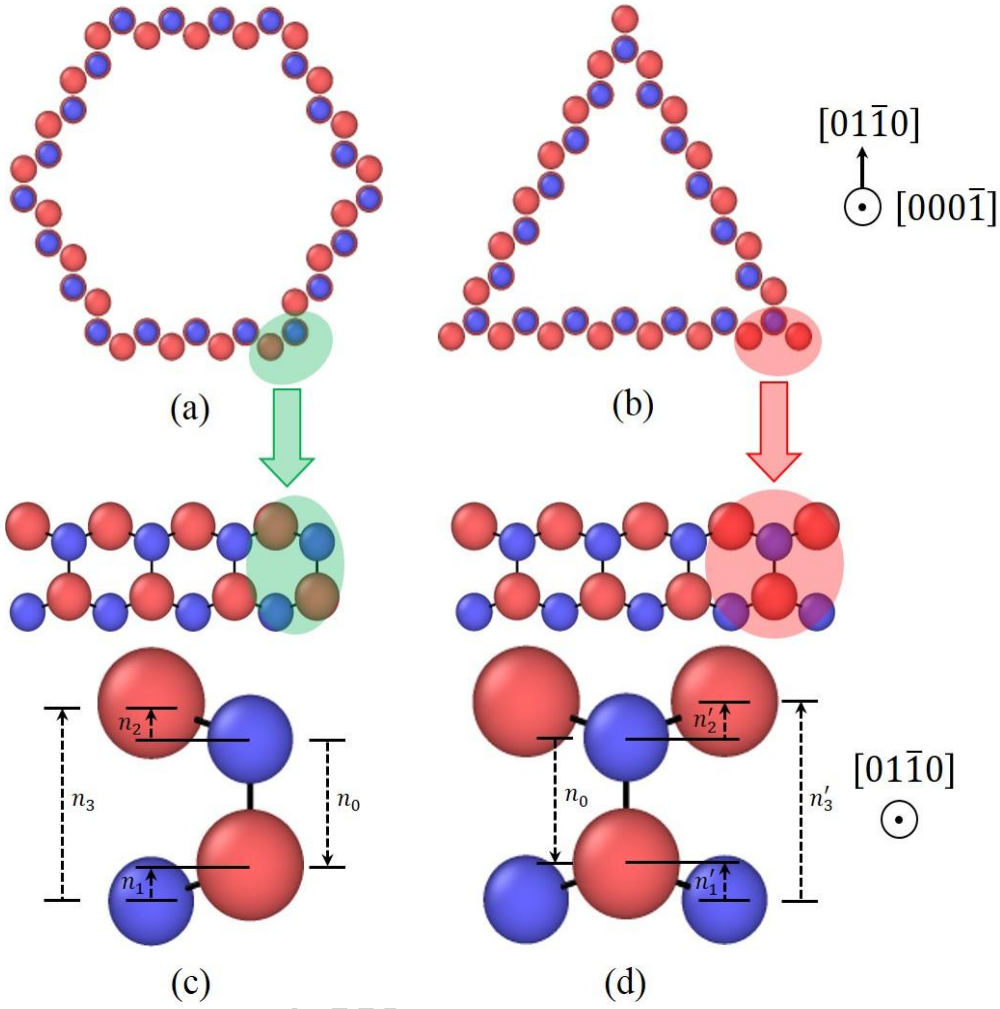

Figure 6. Typical Structure of h-NW and t-NW core layers where the O atoms are colored in blue and Zn atoms in red. a) and b) cross section of h-NW and t-NW core layer structure, viewed along the NW axial $[000\bar{1}]$ direction. c) Structure of the h-NW layer and its corner structure as highlighted in green in a) viewed along the transverse $[01\bar{1}0]$ direction. Here $\boldsymbol{n}_{i\ (i=0-3)}$ show the displacement vectors of the dipoles within the unit where $\boldsymbol{n}_o$ ($[000\bar{1}]$ directed) is negative. d) Structure of the t-NW layer and its corner structure as highlighted in red in b) viewed along the $[01\bar{1}0]$ direction. The displacement vectors of the positive ($[0001]$ directed) dipoles produced by the additional Zn-O pair are labelled by $\boldsymbol{n}'_{i\ (i=1-3)}$.

Accepte

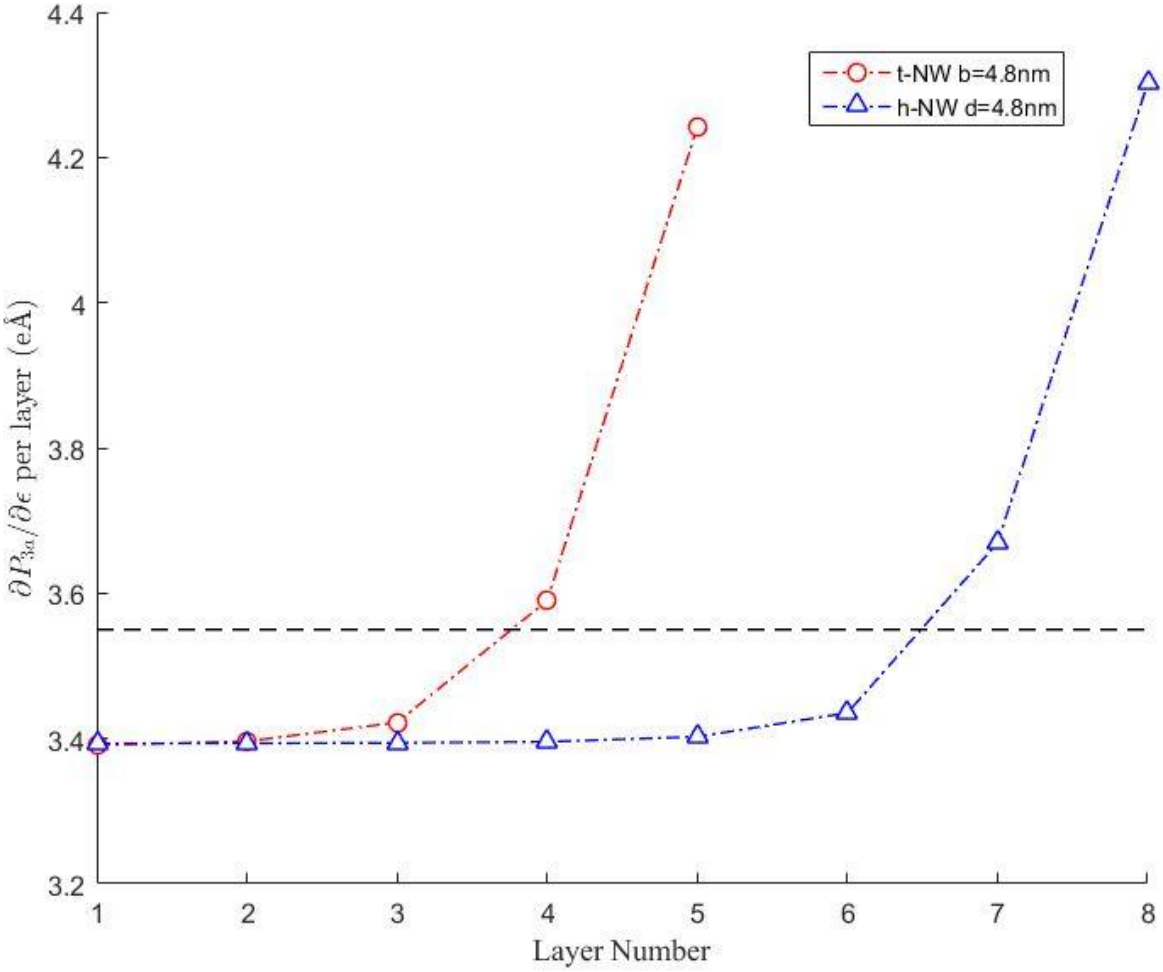

Figure 7. Distribution of $(\partial P_{3a}/\partial \varepsilon_3)^l$ for 4.9 nm h-NW and 4.9 nm t-NW. The additional Zn-O atoms (Fig. 6d) in the t-NW layers have been removed. The horizontal dashed line marks the bulk value of 3.55 eÅ.

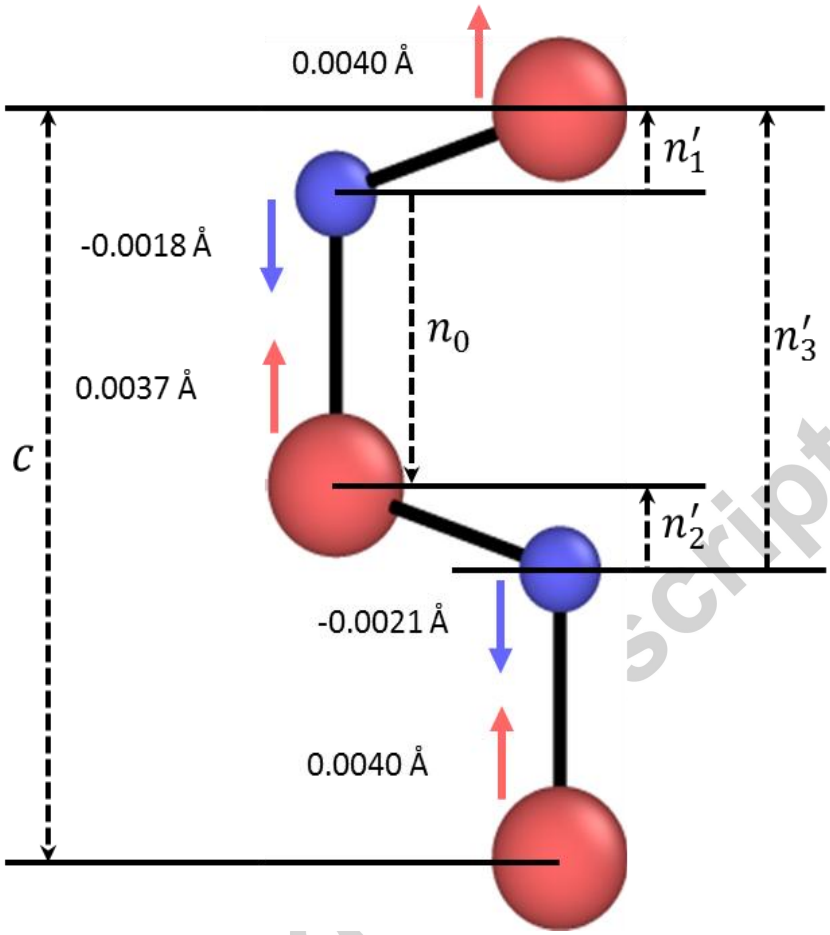

Figure 8. Characteristic relaxation behaviour, at +0.5% strain state, for a primitive wurtzite unit cell from the t-NW core layer corner of Fig. 6b. The atomic displacement (with the affine deformation removed) in the axial direction is marked by the blue arrow nearest to the O atoms (blue) and the red arrow nearest to the Zn atoms (red). This results in a shortening of $\boldsymbol{n}_o$ and lengthening of $\boldsymbol{n}'_{i\ (i=1-3)}$ (refer to Fig. 6). C, the wurtzite [0001] lattice constant, does not change with relaxation due to periodicity. Similar behavior is observed in the h-NW core layers.

Table 1. Characteristic sizes of all ZnO nanostructures examined

h-NW/t-NW	d/b (nm)	h-NT (di = 2 nm)	d_o (nm)	h-NT (di = 4 nm)	d_o (nm)	h-NT (di = 10 nm)	d_o (nm)
1	4.906	1	4.906	5	7.523	8	12.756
2	6.716	2	6.869	6	9.485	9	14.719
3	12.756	3	12.756	7	15.373	10	20.606
4	15.373						
5	20.606						

ACCEPTED MANUSCRIPT

Table 2. Evaluated results of Eqn. 6 for t-NWs, where $A = (\partial P_{3a}/\partial \varepsilon_3) * V_a^{-1}$ and $B = (\partial V_a^{-1}/\partial \varepsilon_3) * P_{3a}$ in units of (C/m^2).

t-NW	$\partial P_{3a}/\partial \varepsilon_3$ (eÅ)	V_a^{-1} (Å^{-3})	A (C/m^2)	P_{3a} (eÅ)	$\partial V_a^{-1}/\partial \varepsilon_3$ (Å^{-3})	B (C/m^2)
4.9 nm	3.981	0.04719	3.010	1.489	-0.01724	-0.411
6.7 nm	3.878	0.04565	2.836	1.409	-0.01753	-0.396
12.8 nm	3.740	0.04388	2.629	1.299	-0.01814	-0.377
15.4 nm	3.710	0.04353	2.587	1.274	-0.01831	-0.374
20.6 nm	3.671	0.04310	2.535	1.242	-0.01857	-0.370

Table 3. Evaluated results of Eqn. 6 for h-NTs, where $A = (\partial P_{3a}/\partial \varepsilon_3) * V_a^{-1}$ and $B = (\partial V_a^{-1}/\partial \varepsilon_3) * P_{3a}$ in units of (C/m^2).

h-NT	$\partial P_{3a}/\partial \varepsilon_3$ (eÅ)	V_a^{-1} (Å^{-3})	A (C/m^2)	P_{3a} (eÅ)	$\partial V_a^{-1}/\partial \varepsilon_3$ (Å^{-3})	B (C/m^2)
1 (d_o=4.9 nm)	3.870	0.05213	3.2321	1.2955	-0.01747	-0.3625
2 (d_o=6.9 nm)	3.699	0.04712	2.7922	1.2266	-0.01846	-0.3627
3 (d_o=12.8 nm)	3.609	0.04399	2.5438	1.1777	-0.01900	-0.3586
4 (d_o=7.5 nm)	3.894	0.05183	3.2333	1.2955	-0.01598	-0.3317
5 (d_o=9.5 nm)	3.704	0.04706	2.7928	1.2261	-0.01826	-0.3586
6 (d_o=15.4 nm)	3.610	0.04400	2.5446	1.1776	-0.01905	-0.3593
7 (d_o=12.8 nm)	3.909	0.05130	3.2133	1.2957	-0.01294	-0.2687
8 (d_o=14.7 nm)	3.709	0.04690	2.7866	1.2258	-0.01760	-0.3457
9 (d_o=20.6 nm)	3.611	0.04398	2.5444	1.1776	-0.01904	-0.3592

Table 4. Evaluated results of Eqn. 6 for h-NWs, where $A = (\partial P_{3a}/\partial \varepsilon_3) * V_a^{-1}$ and $B = (\partial V_a^{-1}/\partial \varepsilon_3) * P_{3a}$ value in units of (C/m^2).

h-NW	$\partial P_{3a}/\partial \varepsilon_3$ (eÅ)	V_a^{-1} (Å^{-3})	A (C/m^2)	P_{3a} (eÅ)	$\partial V_a^{-1}/\partial \varepsilon_3$ (Å^{-3})	B (C/m^2)
4.9 nm	3.668	0.04625	2.718	1.217	-0.01833	-0.357
6.7 nm	3.635	0.04496	2.619	1.196	-0.01857	-0.356
12.8 nm	3.600	0.04353	2.511	1.170	-0.01898	-0.356
15.4 nm	3.587	0.04325	2.485	1.165	-0.01911	-0.357
20.6 nm	3.577	0.04291	2.459	1.159	-0.01927	-0.358

Accepted manuscript

Table 5. e_{33}^{eff} results for finite h-NWs (d = 4.7nm) and t-NWs (b=7nm) of clamped ends, varying aspect ratio and nearly equal specific surface area in units of (C/m^2).

Aspect ratio		1.6	2.1	3.0	5.0	7.8	10.0	∞
e_{33}^{eff} (C/m^2)	h-NW		2.157		2.260		2.335	2.361
	t-NW	2.330		2.385		2.455	2.465	2.441

Table 6 . Evaluated results of Eqn. 6 for h-NWs and NBs with w/t ratio of 2, where $A = (\partial P_{3a}/\partial \varepsilon_3) * V_a^{-1}$ and $B = (\partial V_a^{-1}/\partial \varepsilon_3) * P_{3a}$ value in units of (C/m^2).

h-NW	$\partial P_{3a}/\partial \varepsilon_3$ $(e$Å$)$	V_a^{-1} (Å^{-3})	A (C/m^2)	P_{3a} $(e$Å$)$	$\partial V_a^{-1}/\partial \varepsilon_3$ (Å^{-3})	B (C/m^2)
7.5 nm	3.631	0.04469	2.600	1.191	-0.01862	-0.355
12.1 nm	3.635	0.04361	2.516	1.172	-0.01894	-0.356
NB	$\partial P_{3a}/\partial \varepsilon_3$ $(e$Å$)$	V_a^{-1} (Å^{-3})	A (C/m^2)	P_{3a} $(e$Å$)$	$\partial V_a^{-1}/\partial \varepsilon_3$ (Å^{-3})	B (C/m^2)
7.5 nm	3.651	0.04516	2.642	1.203	-0.02110	-0.407
12.1 nm	3.611	0.04393	2.541	1.180	-0.02078	-0.393

Research Highlights

- Atomistic study of shape effect on piezoelectricity of four nanostructures.
- Identified the physical origin of the shape effect including the fraction of strain-sensitive dipoles, surface piezoelectricity and volume contraction.
- While the latter two are effects of the free surface, the influence of the strain-sensitive dipoles is purely a result of the variation in cross sectional geometry.
- The greatest e_{33}^{eff} is achieved for h-NTs at small size and t-NWs at large size (critical size of ~7nm). e_{33}^{eff} of h-NWs and NBs are close but always lower than e_{33}^{eff} of h-NTs and t-NWs.

Accepted manuscript

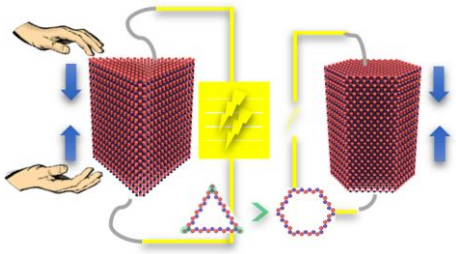

Graphical abstract

Accepted manuscript